Chapter 3

Reversible, equilibrium interconversion of an iron cyanide and an iron aminocarbyne via an H-bond mediated proton-coupled electron transfer

3.1 Introduction

The storage of chemical energy as solar fuels has motivated the development of proton-coupled reductions of small molecules at ambient conditions and low applied overpotential.[1,2] This effort requires catalysts that lower the kinetic barriers and level the energy between intermediates , as well as strategies to deliver multiple H^+/e^-.[3] Considerable progress has been made towards the reversible interconversion of $2H^+/2e^-$ energy carriers (e.g., H^+/H_2, CO_2/HCO_2H, CO_2/CO, O_2/H_2O_2) with molecular,[4,5,6,7,8,9] heterogeneous[10,11] and enzymatic examples.[12,13,14,15] By contrast, examples of the deep (> 2 e^-) reductions of small molecule triple bonds, N_2 or CO,[16,17,18,19,20,21,22,23] which would yield desirable energy carriers, like NH_3 or CH_3OH, require a considerable thermodynamic driving force at ambient conditions. Likewise, the corresponding oxidation reactions, ammonia and methanol oxidation requires a large driving force.[24,25,2627,28,29,30] The lowest driving force conditions reported for N_2 reduction to NH_3 (Nitrogen reduction, N_2R) and oxidation of NH_3 to N_2 (ammonia oxidation, AO) occur at an overpotential of ~80 kcal mol^{-1} per equiv N_2 (Scheme 3.1).[18,26]

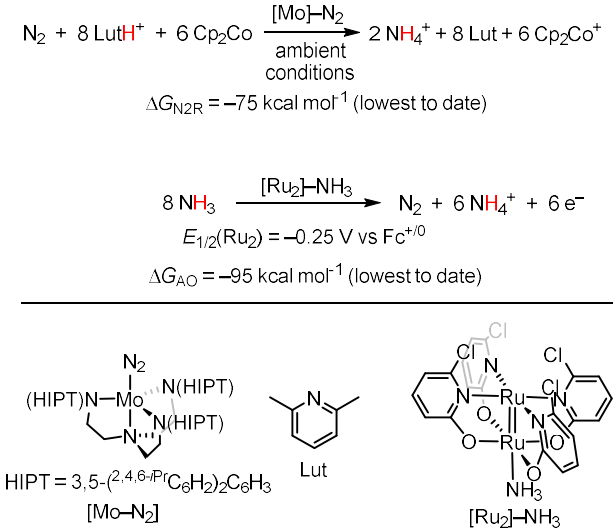

Scheme 3.1. Lowest overpotential catalytic N_2R and AO with molecular complexes reported to date.[18,26]

As a complementary approach to the study of these catalytic reactions, the development and characterization of systems that can undergo multiple reversible H^+/e^-

transfers during triple bond activation might aid the development of new strategies for efficient small molecule reduction. Pioneering studies by Meyer and coworkers have demonstrated multiproton-and-electron reversible interconversions of transition metal oxos with the corresponding aquo complexes.[31,32] However, examples of reversible reduction of transition metal activated small molecule triple bonds are limited to the $2H^+/2e^-$ reduction of Os-bound MeC≡N to the corresponding imine (Figure 3.1).[33] The bidirectional $2H^+/2e^-$ interconversion of a tungsten cyanide complex (W(CN)) and the corresponding aminocarbyne (W(CNH_2)) (Figure 3.1), provides another notable example of triple bond activation.[34] However, this reaction does not occur at equilibrium, requiring a $\Delta E > 1$ V between the oxidative and reductive reactions.

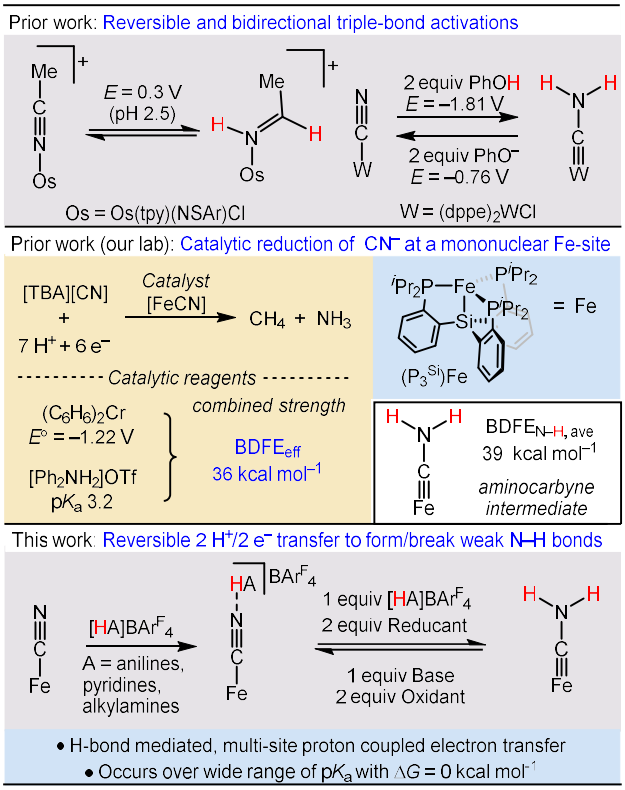

Figure 3.1. Background on reversible small molecule activation and CN^- reduction as context for this study.[23,33,34,36]

Our laboratory recently reported conditions for the catalytic, 7 H^+/6 e^- reduction of [TBA][CN] to CH_4 and NH_3 at a mononuclear iron tris(phosphino)sylil platform, $P_3^{Si}Fe$ (abbreviated as [Fe] throughout this report), using $(C_6H_6)_2Cr$ and $[Ph_2NH_2]OTf$ as e^- and H^+

source, respectively (Figure 3.1, middle).[23] In this study, the $2H^+/2e^-$ reduction product of the [Fe−C≡N] precatalyst,[35] a terminal iron aminocarbyne [Fe≡C−NH_2], was observed as a catalytic intermediate (Figure 3.1, middle). Aminocarbyne formation occurred at a mild thermodynamic overpotential[36] and despite weak N−H bonds (Figure 3.1) the aminocarbyne was stable at low temperature (−80 °C). The close BDFE matches of the species (Figure 3.2) indicate an energy match between [FeCN], [FeCNH] and [$FeCNH_2$]. These attributes suggested the $2H^+/2e^-$ equilibration of [FeCN]↔[$FeCNH_2$] might be observable and could provide an interesting point of comparison for early N−H bond formation in N_2R (nitrogen reduction).[36,37]

Reversible interconversion of [FeCN]↔[$FeCNH_2$], would require reagents that can approach both the reductive ([FeCN]→[$FeCNH_2$]) and oxidative ([$FeCNH_2$]→[FeCN]) proton-coupled redox reactions at minimal driving force. In the catalytic conditions, reduction of [FeCN] (pK_a 5.6, all pK_a's in THF, Figure 3.2) occurred via initial proton transfer (PT) to [FeCN] by the strong acid [Ph_2NH_2]OTf (pK_a 3.2).[23,36] However, as proton-coupled oxidation of [$FeCNH_2$] would require a base capable of deprotonating $[FeCNH_2]^+$ (the related methylated analogue $[FeCN(H)Me]^+$ has pK_a 7.1), we initially sought alternative strategies to reduce [FeCN] utilizing weaker acids.

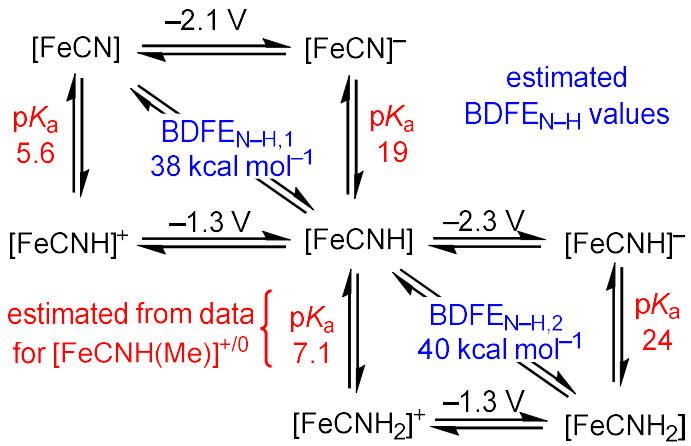

Figure 3.2. Pertinent thermochemical measurements for [FeCN], [FeCNH(Me)] (as a model for [$FeCNH_2$]), and relevant intermediates. Values are measured in THF at 25 °C.[36]

Noting that H-bonding to terminal cyanide ligands is well-established,[38] and H-bonds, in turn, can facilitate multisite-proton coupled electron transfers (MS-PCET),[39] pathways with lower enthalpic barriers than stepwise alternatives,[40,41,42] we targeted such a strategy for [FeCN] reduction.

$$\mathrm{BDFE_{eff}} = 23.06\,E^{\circ} + 1.37\ \mathrm{p}K_a + C_{\mathrm{G}} \quad \text{(eqn 3.1)}$$

$$\Delta G = 2\ \mathrm{BDFE_{eff}} - (\mathrm{BDFE_{N-H,1}} + \mathrm{BDFE_{N-H,2}}) \quad \text{(eqn 3.2)}$$

MS-PCET strategies also allow ready tuning of the thermodynamic driving force by decoupling acid/base and reductant/oxidant pairs.[39,40] The combined reagent strength can be estimated using the effective bond dissociation free energy ($BDFE_{eff}$; eqn 3.1), a measure of the net thermodynamic H-atom donor ability of a reagent pair, with inputs E(reductant/oxidant), pK_a(acid/base), and a solvent and temperature dependent constant C_G, which is 59.9 kcal mol^{-1} in THF at 25 °C.[43,44] Comparing the $BDFE_{eff}$ to the $BDFE_{N-H}$ of [FeCN−H] (38 kcal mol^{-1}) and [FeCN(Me)−H] (40 kcal mol^{-1}; an analogue of [$FeCNH_2$]) allows for an estimate of driving force (ΔG; eqn 3.2) for [$FeCNH_2$] formation, and a helpful metric for choosing reagents that might allow an equilibrium reaction. Using these principles, we develop the rapid equilibrium $2H^+/2e^-$ interconversion between [FeCN] and [$FeCNH_2$] (Figure 3.1, bottom).

3.2 Results

3.2.1 Characterization and reduction of H-bonded adduct to [FeCN]

To target H-bond formation between [FeCN] and acid, we wanted to remove competitive Brönsted basic sites in solution (e.g., solvent, counteranion), thereby favoring acid coordination to N_{CN}.[45]

The addition of [$PhNH_3$]BAr^F_4 (pK_a 8.0)[46] to [FeCN] in Et_2O at −80 °C resulted in a color change from red to purple. This color change can be monitored by UV-vis with the diagnostic d-d transition of [FeCN] (absorption maxima: 530 nm, 909 nm, Figure B.1) shifting slightly (new maxima: 550 nm and 895 nm), but less than upon the full protonation

to [FeCNH]BAr^F_4 (absorption maxima: 600 nm and 790 nm). ^{57}Fe Mössbauer of the frozen mixture of [^{57}FeCN] + 2.5 equiv [$PhNH_3$]BAr^F_4 showed a single new species with Mössbauer parameters $\delta = 0.44$ mm s^{-1} and $\Delta E_Q = 2.06$ mm s^{-1} (Figure 3.3), similar, but distinctly shifted from starting material, [^{57}FeCN] ($\delta = 0.44$ mm s^{-1} and $\Delta E_Q = 1.77$ mm s^{-1}). IR data shows a slight shift in $\nu_{C\equiv N}$ upon adding acid (2075 cm^{-1}, compared to 2082 cm^{-1} in the absence of acid), consistent with slight activation of the CN^- ligand. These data together support the formation of an H-bonded adduct, [$FeCN\cdots HNH_2Ph$]BAr^F_4.

With this H-bonded complex in hand, we explored its reductive chemistry. The addition of 2.5 equiv Cp^*_2Cr ($E(Cr^{III/II})$=−1.47 V)[47] to a solution of [FeCN] and 2.5 equiv [$PhNH_3$]BAr^F_4 at −80 °C in Et_2O was monitored by UV-vis and rapid consumption ($\tau_{1/2}$ <10 s) of [$FeCN\cdots HNH_2Ph$]$^+$ was observed, with a new shoulder growing in at 590 nm, consistent with the formation of [$FeCNH_2$] (Figure B.13). As we have previously observed, the aminocarbyne is stable at −80 °C, but under these conditions, upon warming to 0 °C, it decays to reform [FeCN]. Monitoring this reaction by ^{57}Fe Mössbauer spectroscopy confirmed the formation of [$FeCNH_2$] with the parameters δ = 0.04 mm s^{-1} and ΔE_Q = 0.98 mm s^{-1}, diagnostic for the aminocarbyne (Figure 3.3).[23]

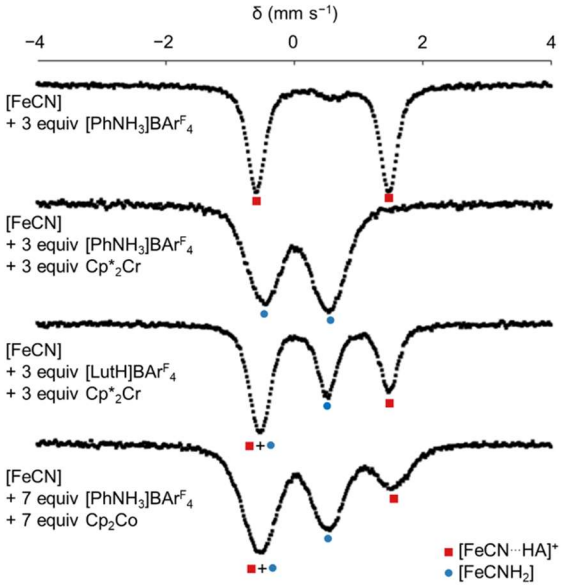

Figure 3.3. ^{57}Fe Mössbauer spectra of selected reactions of [FeCN] with acid and reductant.[48]

Interestingly, the first N−H bond formation, converting [FeCN] to [FeCN−H], cannot be (readily) accounted for via stepwise proton and electron transfers, as $[PhNH_3]^+$ is not acidic enough to protonate [FeCN] and Cp^*_2Cr does not reduce [FeCN] (Figure 3.2). Along with the observed H-bonded complex, these observations align with our initially posited MS-PCET reaction, although kinetic studies (*vide infra*) provided more reliable evidence of this mechanism.

This reagent combination is competent for reducing [FeCN] to release NH_3: reacting [FeC^{15}N] with 20 equiv Cp^*_2Cr and 20 equiv $[PhNH_3]OTf$ yields $^{15}NH_3$ (0.2 equiv NH_3/Fe). However, these yields are much lower than for the reduction of [FeCN] by the catalytic reagents $[Ph_2NH_2]OTf$ and $(C_6H_6)_2Cr$ (0.75 equiv NH_3/Fe). [23]

Table 3.1. Comparison of reagent strengths and the observation of aminocarbyne formation.

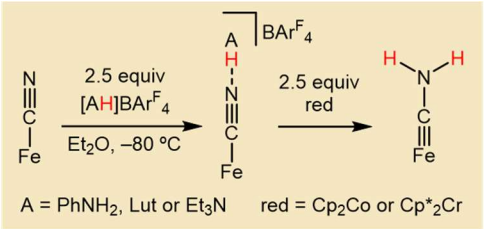

Reagent strength:		$BDFE_{eff}$ (kcal mol^{-1})	ΔG (kcal mol^{-1})	
Cp^*_2Cr (−1.47 V)	$[PhNH_3]BAr^F_4$ (pK_a 8.0)	37	−5	Complete formation of $[FeCNH_2]$
Cp^*_2Cr (−1.47 V)	$[LutH]BAr^F_4$ (pK_a 9.5)	39	−1	Partial formation of $[FeCNH_2]$
Cp_2Co (−1.33 V)	$[PhNH_3]BAr^F_4$ (pK_a 8.0)	40	+2	Partial formation of $[FeCNH_2]$
Cp_2Co (−1.33 V)	$[LutH]BAr^F_4$ (pK_a 9.5)	42	+6	No reaction
Cp^*_2Cr (−1.47 V)	$[Et_3NH]BAr^F_4$ (pK_a 13.7)	45	+11	No reaction

3.2.3 Thermodynamics of aminocarbyne formation

With the rapid reduction of [FeCN] to $[FeCNH_2]$ established, we used eqn 3.1 and 3.2 to assess reaction thermodynamics. For the combination Cp^*_2Cr ($E(Cr^{III/II}) = –1.47$ V)[23] and $[PhNH_3]^+$ (pK_a 8.0)[46] the $BDFE_{eff}$ = 37 kcal mol^{-1}, giving ΔG = –5 kcal mol^{-1} (Table 3.1). Reductions with either slightly weaker acid or reductant would shift ΔG towards 0.

Accordingly, reacting [^{57}FeCN] with 3 equiv [LutH]BAr^F_4 (Lut = 2,6-dimethylpyridine; pK_a 9.5)[46] followed by 3 equiv Cp^*_2Cr in Et_2O at −80 °C, freeze-quenching and analyzing by ^{57}Fe Mössbauer spectroscopy revealed two major species formed in about a 1:1 ratio, assigned as [$FeCNH_2$], and [$FeCN^{\cdots}HLut]^+$ (Figure 3.3 and Table 3.1). The observation of unconsumed starting material is consistent with this reaction's small, estimated driving force (ΔG = −1 kcal mol^{-1}; Table 3.1).[49] Alternatively, the reaction of [^{57}FeCN] with 7 equiv Cp_2Co (cobaltocene; $E(Co^{III/II})$=–1.33 V)[23] and 7 equiv [$PhNH_3$]BAr^F_4 at −80°C similarly analyzed by ^{57}Fe Mössbauer also shows a mixture of [$FeCNH_2$] and [$FeCN^{\cdots}HNH_2Ph]^+$ (Figure 3.3 and Table 3.1; ΔG = +2 kcal mol^{-1}).[50]

As expected, when the $BDFE_{eff}$ is increased further using either Cp^*_2Cr/[Et_3-NH]BAr^F_4 (ΔG = +11 kcal mol^{-1}, Table 3.1 and Figure B.18) or Cp_2Co/[LutH]BAr^F_4 (ΔG = +6 kcal mol^{-1}, Table 3.1 and B.14) no reduction of [FeCN] was observed by UV-vis.

3.2.3 Establishing reversibility

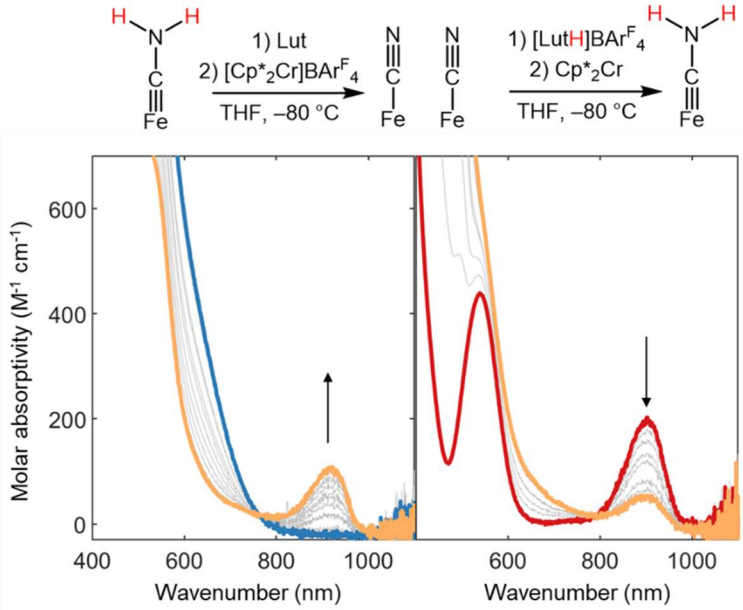

Figure 3.4. Reversible interconversion of iron cyanide and iron aminocarbyne. (Top) UV-vis titration of [Cp^*_2Cr]BAr^F_4 (4.5 mM) into 1.5 mM [$FeCNH_2$] with Lut (4.5 mM), at −80°C in THF. (Bottom) UV-vis titration of Cp^*_2Cr (4.5 mM) into 1.5 mM [FeCN] with [LutH]BAr^F_4 (4.5 mM) at −80°C in THF.

Having demonstrated that the $2H^+/2e^-$ reduction of [FeCN] to [$FeCNH_2$] can occur at $\Delta G \approx 0$, we attempted the reverse, proton-coupled aminocarbyne oxidation to confirm a bidirectional reaction. We have previously developed the *in situ* synthesis of [$FeCNH_2$] with [K]BAr^F_4 via the low temperature (−80°C) double protonation of generated [FeCN]K_2 (see appendix section B.2.2 for details).[23] Generation of [$FeCNH_2$] in this fashion in THF,[51] followed by addition of Lut (3 equiv), and finally the titration of [Cp^*_2Cr]BAr^F_4 (0 to 3 equiv), we observed the growth of a feature around 900 nm associated with formation of [FeCN···H−Lut]BAr^F_4, demonstrating the oxidation of [$FeCNH_2$] →[FeCN] (Figure 3.4, left panel). However, only partial oxidation is observed, consistent with a reaction close to equilibrium. The isosbestic point at about 790 nm indicates a clean transformation. To confirm that this reaction was occurring at equilibrium, we also assessed the reductive reaction under identical conditions. Cp^*_2Cr was titrated into a mixture of [FeCN] and 3 equiv [LutH]BAr^F_4 in THF at – 80 °C, observing now a partial bleaching of the diagnostic feature at 900 nm and an isosbestic point at 790 nm (Figure 3.4, right panel).

Both the oxidative and reductive titrations establish mixtures of [FeCN] and [$FeCNH_2$], consistent with the ΔG ~0 for the [LutH]BAr^F_4/Cp^*_2Cr reagent pair. This confirms this reaction as a $2H^+/2e^-$ reversible equilibrium.

3.2.4 Exploring a wider range of reagent strengths

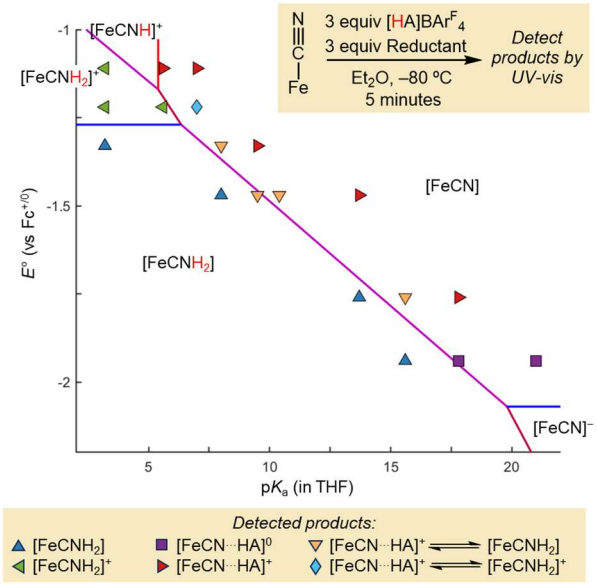

Figure 3.5. Pourbaix diagram for reaction of 2 equiv reductant and acid with [FeCN]. Markers show observed products, while lines indicate predicted products based on the previously measured thermochemistry.

With equilibrium reversibility between [FeCN] and [FeCNH$_2$] established, we next explored the reduction of [FeCN] over a wider range of acid and reductant strengths by UV-vis spectroscopy. To solutions of [FeCN] at −80°C in Et$_2$O, acids (pK_a 3.2 – 21) and reductants ($E°_{red}$ = −1.22 V to −1.96 V) of varying strength were added. Over this range, we observed a variety of [FeCN] reduction products, which can be plotted against the reagent strengths as a Pourbaix diagram (Figure 3.5). In short, our previously measured thermochemistry accurately predicts the observed products, albeit with some interesting deviations (*vide infra*).

Using strong acids and relatively weak reductants, such as [Ph$_2$NH$_2$]BAr$^F_4$/(C$_6$H$_6$)$_2$Cr or Cp$_2$Cr (E(Cr$^{III/II}$)=−1.11 V), the cationic aminocarbyne, [FeCNH$_2$]BAr$^F_4$, is the major product. This is in line with our previous report, where only upon addition of a larger excess of (C$_6$H$_6$)$_2$Cr is the [FeCNH$_2$]$^{+/0}$ reduction accessed.[23] Neither of these reductants are of sufficient strength to reduce [FeCNH]$^+$ (E(Fe$^{II/III}$) =−1.27 V, Figure 3.2), however, the

presence of excess $[Ph_2NH_2]BAr^F_4$ should give rapid protonation of *in situ* formed $[FeCNH]^0$, driving product formation towards $[FeCNH_2]^+$, the favored product.

As stronger reductants and weaker acids are used, $[FeCNH_2]$ becomes the favored product and varying the acid pK_a from 8.0-15.4, if paired with a reductant of sufficient strength such that $BDFE_{eff} \approx 39$ kcal mol^{-1} an equilibrium of $[FeCN] \leftrightarrow [FeCNH_2]$ is established. The relationship between reagent strength and products is consistent, with 59.4 mV/ΔpK_a expected for a $2H^+/2e^-$ transfer. Notably, despite these thermochemical measurements being made in THF at 25 °C, the values reasonably accurately predict reactivity in Et_2O at –80 °C. Considering that reagent strengths are often measured at 25 °C, while many reactions, such as Fe-based N_2R, are performed at lower temperatures[17,52] these results demonstrate that room temperature thermochemical values can still accurately predict reaction products.

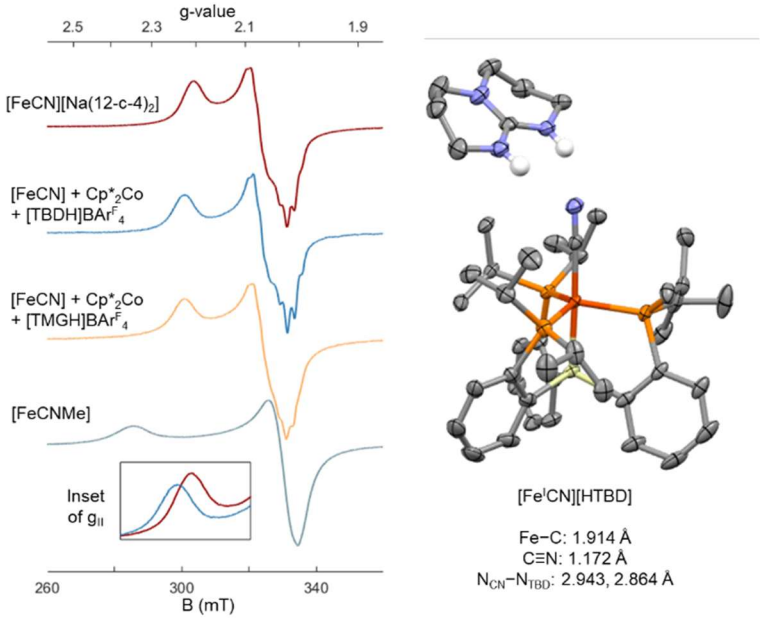

Figure 3.6. Formation of $[Fe^ICN][HTBD]$. (Left) EPR spectra of $[Fe^ICN][HTBD]$ and $[Fe^ICN][HTMG]$ with reference complexes $[Fe^ICN][Na(12\text{-c-}4)_2]$ and $[Fe^ICNMe]^0$. (Right) Solid-state structure of [FeCN][HTBD] with thermal ellipsoids displayed at 50% probability, H-atoms except H-bonding protons omitted for clarity.

Our previous thermochemical measurements do not predict the reactivity of [FeCN] with weak acids (pK_a >18) and strong reductants ($E(red^{+/0}) \sim -2.0$ V). Reacting [FeCN] with

Cp^*_2Co (decamethylcobaltocene; $E(Co^{III/II})$ = −1.96 V)[52] and $[TBDH]BAr^F_4$ (TBD = Triazabicyclodecene, pK_a 21)[46] results in partial consumption of starting material (Figure B.24), despite the thermochemical measurements suggesting no reaction should occur (ΔG = +9 kcal mol^{-1}). Analysis by continuous wave-EPR (cw-EPR) demonstrates that the product is not $[FeCNH_2]$ but a new S = ½ species. The freeze-quenched reaction of [FeCN] with Cp^*_2Co and $[TBDH]BAr^F_4$ generates a spectrum similar to $[FeCN][Na(12\text{-c-}4)_2]$.[35] However, a slight shift in $g_\parallel$ ($g_\parallel$ = 2.23 compared to $g_\parallel$ = 2.21 for $[FeCN][Na(12\text{-c-}4)_2]$, Figure 3.6A) is observed, suggesting mild activation of the CN^- ligand. This degree of activation is much less than for the previously characterized *bona fide* iron isocyanide [FeCNMe].[36]

We posited that these observations could be attributed to the formation of H-bonded adduct to $[FeCN]^-$ ($[Fe^ICN\cdots HTBD]^0$), resulting in a slightly activated CN^- ligand, which also shifts the $E°(Fe^{I/II})$, such that more Fe^I is observed. This assignment was confirmed by independent synthesis of the adduct $[Fe^ICN\cdots HTBD]^0$ via the low-temperature addition of [TBDH]OTf to $[FeCN][Na(12\text{-c-}4)_2]$, which allowed crystallization and analysis by XRD (Figure 3.6B). Particularly diagnostic was the C−N bond length of this new adduct (1.172 Å), which is much closer to $[FeCN][Na(12\text{-c-}4)_2]$ (1.170 Å)[35] than [FeCNMe] (1.186 Å).[36] The short distance between N_{CN} and N_{TBD} (2.94 and 2.86 Å) is consistent with an H-bond interaction between the acid and $[FeCN]^-$.[53] This complex also displays an activated $\nu_{C\equiv N}$ (1978 cm^{-1} compared to 2014 cm^{-1} for $[FeCN][Na(12\text{-c-}4)_2]$).

$[TMGH]BAr^F_4$, which should establish an equilibrium mixture of $[FeCN]\leftrightarrow[FeCNH_2]$ (ΔG = +0.6 kcal mol^{-1}), instead also generates a similar cw-EPR spectrum (Figure 3.6A), with a slightly shifted $g_\parallel$, suggesting that this reduced H-bonded adduct can also be favored over full N−H bond formation.

3.2.5 Probing electrochemical reversibility

Given the precedent for electrochemically reversible multiproton-and-electron activations we were motivated to explore electrochemical reductions of [FeCN] as well. The cyclic voltammogram (CV, Figure 3.7, blue trace) of [FeCN] (1 mM) in 0.2 M $[TBA]PF_6$ in

THF displays to two reversible redox couples, an oxidative $E(Fe^{II/III})$ = −0.38 V and a reductive feature $E(Fe^{I/II})$ = −2.07 V.[35] Upon the addition of [$PhNH_3$]OTf (pK_a 8.0; 5 to 20 equiv, Figure 3.7 red trace and Figure B.64), the reductive peak shifts to E = −1.31 V. The charge passed in this new couple is about ~ 2x that of $[FeCN]^{+/0}$ or $[FeCN]^{0/-}$ couples, consistent with a $2e^-$ redox reaction. This transformation occurs at $BDFE_{eff}$ = 40 kcal mol^{-1}, similar to $BDFE_{N-H,\ ave}$. As expected for an electrochemical H^+/e^- transfer the redox couple is sensitive to the addition of base, shifting cathodically when increasing the amount of [$PhNH_2$] (Appendix B). These observations are all consistent with the 2 e^- reduction expected for the interconversion of [FeCN]/[$FeCNH_2$].

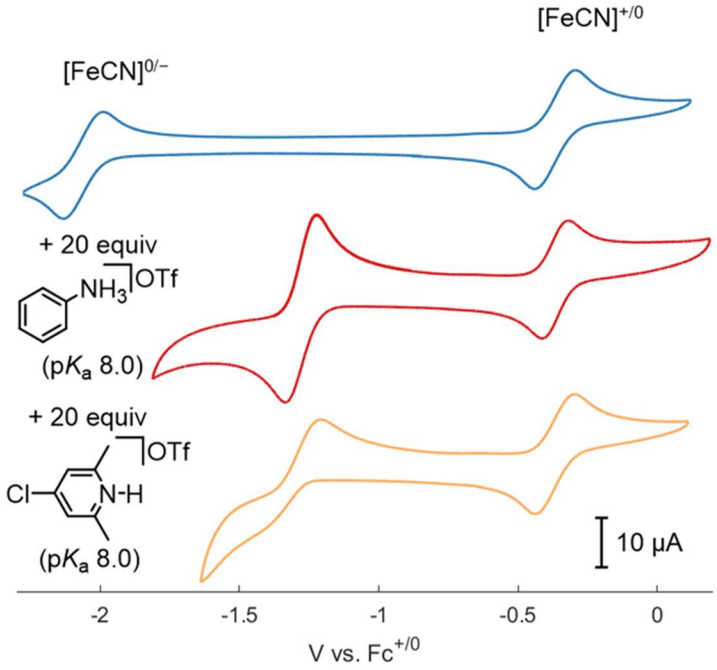

Figure 3.7. Cyclic voltammogram of [FeCN] 1 mM (blue trace) with 20 equiv [$PhNH_3$]OTf (red trace) or [$^{4\text{-Cl-2,6-Me}}$pyrH]OTf (yellow trace) added. All voltammograms collected in in 0.2 M [TBA][PF_6] in THF at 100 mV s^{-1} scan rate.

Unlike the chemical reductions which can be described by simple thermodynamic equations (eqn 3.1 and 3.2) over a large pK_a/E_{red} range, the electrochemical reduction of [FeCN] is highly sensitive to acid choice (Figure B.63). As an example, addition of 20 equiv [$^{4\text{-Cl-2,6-Me}}$pyrH]OTf (pK_a 8.0, Figure 3.7, yellow trace) to [FeCN] , despite having the same pK_a as $[PhNH_3]^+$, does not yield a fully reversible 2 e^- couple by CV. We note that these

electrochemical measurements are conducted at 25 °C in a more coordinating solvent in the presence of electrolyte, all factors that should disfavor H-bond formation. Hypothesizing that this might contribute to the lack of reversibility with [$^{4\text{-Cl-2,6-Me}}$pyrH]OTf we measured the $K_{\text{H-bond}}$ (eqn 3.3) with [$PhNH_3$]OTf and [$^{4\text{-Cl-2,6-Me}}$pyrH]OTf in THF at 25 °C with 0.2 M [TBA][PF_6] to reveal a stronger $K_{\text{H-bond}}$ with [$PhNH_3$]$^+$ ($K_{\text{H-bond}}(PhNH_3^+)$ = 60 ± 10 M^{-1}; $K_{\text{H-bond}}(^{4\text{-Cl-2,6-Me}}pyrH^+)$ = 20 ± 5 M^{-1}).

$$K_{\text{H-bo}} \quad (\text{HA}) = \frac{[\text{FeCN}\cdots\text{HA(OTf)}]}{[\text{FeCN}][\text{HA(OTf)}]} \quad \text{(eqn 3.3)}$$

Consistent with this weaker H-bonding pre-equilibrium, the cyclic voltammogram of [FeCN] in the presence of [$^{4\text{-Cl-2,6-Me}}$pyrH]OTf approaches reversibility as the acid loading is increased further (Figure B.67).

3.2.6 Kinetics of [FeCN] reduction

Finally, we wanted to study the mechanism of reduction of [FeCN] to [$FeCNH_2$] with intermediate strength acid/reductant, such as the initially described Cp^*_2Cr/[$PhNH_3$]BAr^F_4 combination.[54] As previously noted, [FeCN] reduction with these reagents is rapid at −80 °C. To slow the reaction rate, we switched the solvent to a eutectic mixture of 4:1 2-MeTHF:THF, which has a freezing point of −160 °C and sufficient viscosity at −145 °C to study this transformation.[55] Under these conditions, we found that Cp^*_2Cr is insufficiently soluble for kinetic studies; we therefore turned to a more soluble reductant of comparable strength, $^{Et}Cp_2Co$ (1,1-diethylcobaltocene; $E(Co^{III/II})$ = −1.45 V; Figure B.69). The addition of $^{Et}Cp_2Co$ in pseudo-first order excess via syringe to a solution of [FeCN] (1.2 mM) and [$PhNH_3$]BAr^F_4 (3.6 mM) showed complete consumption of the diagnostic [FeCN] peak at 895 nm within 120 s (Figure 3.8A). Plotting of ln(abs_{895}) vs time demonstrated this reaction to be first order in [FeCN] (Figure 3.8B), and use of [$PhND_3$]BAr^F_4 showed a small, normal kinetic isotope effect (KIE) of 1.4±0.1.

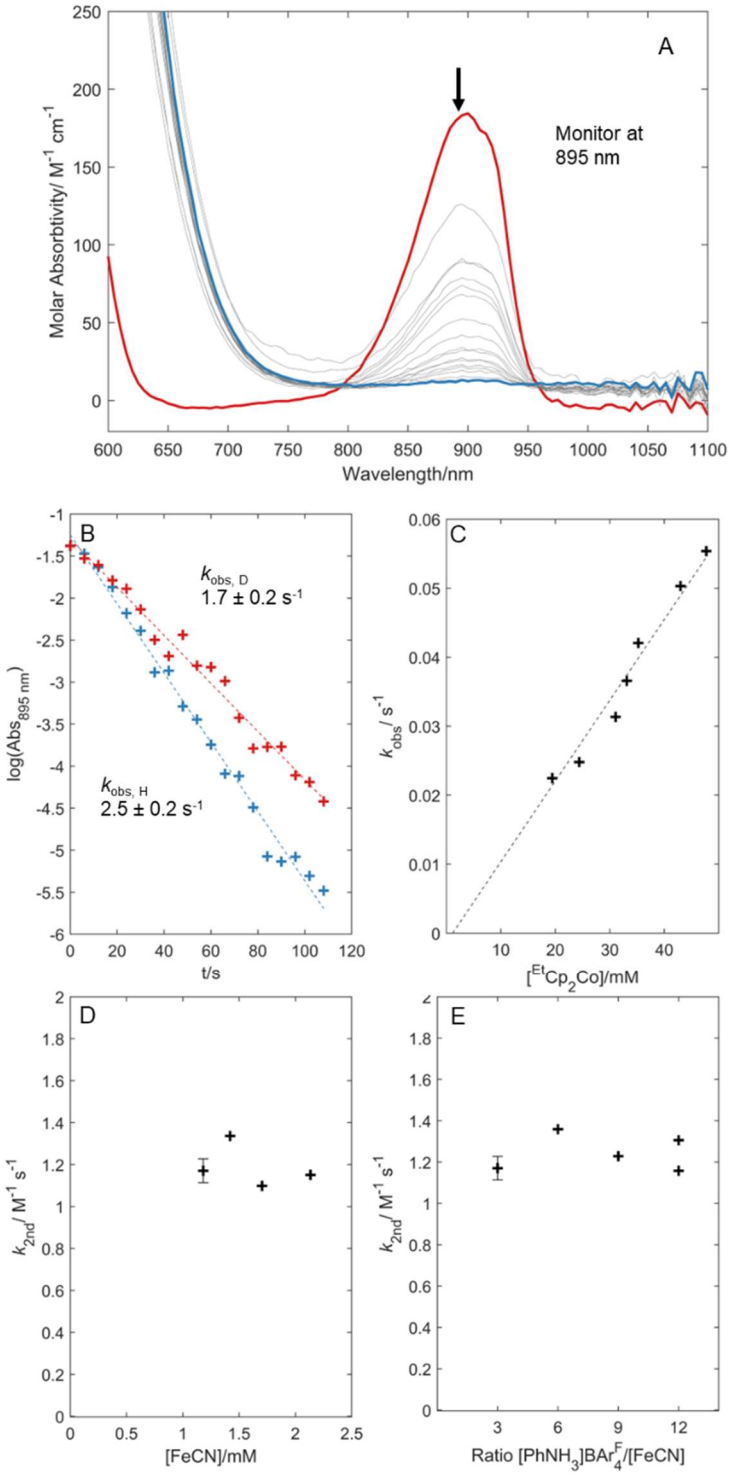

Figure 3.8. Kinetic data for reaction of [FeCN] with $[PhNH_3]BAr^F{}_4$ and $^{Et}Cp_2Co$. All data presented collected at -145 °C in 4:1 2-MeTHF:THF (A) $[FeCN\cdots HNH_2Ph]BAr^F{}_4$ (red trace) is reduced upon addition of $^{Et}Cp_2Co$ (Grey traces every 2 seconds, blue trace after

120 s). (B) Plot of log(Abs$_{[FeCN]}$) against time using either [PhNH$_3$]BAr$^F_4$ (Blue trace) or [PhND$_3$]BAr$^F_4$ (Red trace) with 1.2 mM [FeCN] and 25 equiv ^{Et}Cp$_2$Co. (C) k_{obs} for 1st order decay of [FeCN$\cdots$HNH$_2$Ph]BAr$^F_4$ upon addition of [^{Et}Cp$_2$Co] plotted against [^{Et}Cp$_2$Co]. (D) k_{2nd} plotted against starting [FeCN] concentration. The ratio of [PhNH$_3$]BAr$^F_4$:[FeCN] was kept constant (at 3). (E) k_{2nd} plotted against [FeCN] to [PhNH$_3$]BAr$^F_4$ ratio. Error bars for the 1st data point in plots (E) and (F) represent errors for the 2nd order rate constant determined from the slope in (C).

The pseudo-first order rate constant showed dependence on the reductant concentration, but not [FeCN] or the [PhNH$_3$]BAr$^F_4$:[FeCN] ratio (Figure 3.8C-E and Figure 3.9A) consistent with a rate law = k_2[^{Et}Cp$_2$Co][FeCN], where k_2 =1.17±0.07 M^{-1} s^{-1}. A mechanistic model consistent with these observations is the 1st reduction event being rate limiting with partial proton transfer also occurring in this rate-limiting step (Figure 3.9B). However, since the reaction is independent [PhNH$_3$]BAr$^F_4$:[FeCN] ratio, this would require a pre-association of the acid and [FeCN], e.g., through H-bond formation. This supports an H-bond mediated MS-PCET to form the 1st N−H bond as the rate-limiting step of aminocarbyne formation (Figure 3.9B).

As the 1st N−H bond formation is the rate-limiting step, it is difficult to study the mechanism of the 2nd N−H bond formation. Nonetheless, two mechanisms seem plausible, likely depending on the specific reagent combinations (Figure 3.9C). For combinations of strong acids and weak reductants (e.g., [PhNH$_3$]BAr$^F_4$/^{Et}Cp$_2$Co), we would expect a PT-ET mechanism to form the 2nd N−H bond, with [FeCNH] being rapidly protonated to give [FeCNH$_2$]$^+$, which can be reduced to [FeCNH$_2$]. The acidity of [FeCN(H)Me]$^+$ (pK_a 7.1) provides a useful guide as to what acids might access this protonation. However, reagent combinations utilizing weak acids and strong reductants to form [FeCNH$_2$] (e.g., [pyrrH]BAr$^F_4$/(^{Me4}Cp)$_2$Co; pyrr = pyrrolidine, ^{Me4}Cp = tetramethylcyclopentadienyl), this 2nd protonation should not be accessible, nor should reduction of the intermediate [FeCNH] to [FeCNH]$^-$ (Figure 3.2).[56] Instead, we propose the disproportionation of *in situ* formed [FeCNH] to yield 0.5 equiv [FeCN] and 0.5 equiv [FeCNH$_2$], similar to what we have previously observed for [FeNN−H].[36] Accordingly, attempts to generate [FeCNH]^0 in solution via reduction of [FeCNH]$^+$, protonation of [FeCN]$^-$ or deprotonation of [FeCNH$_2$]$^+$ rapidly converge to 1:1 mixtures of [FeCN]:[FeCNH$_2$] (see appendix section B.2.3).

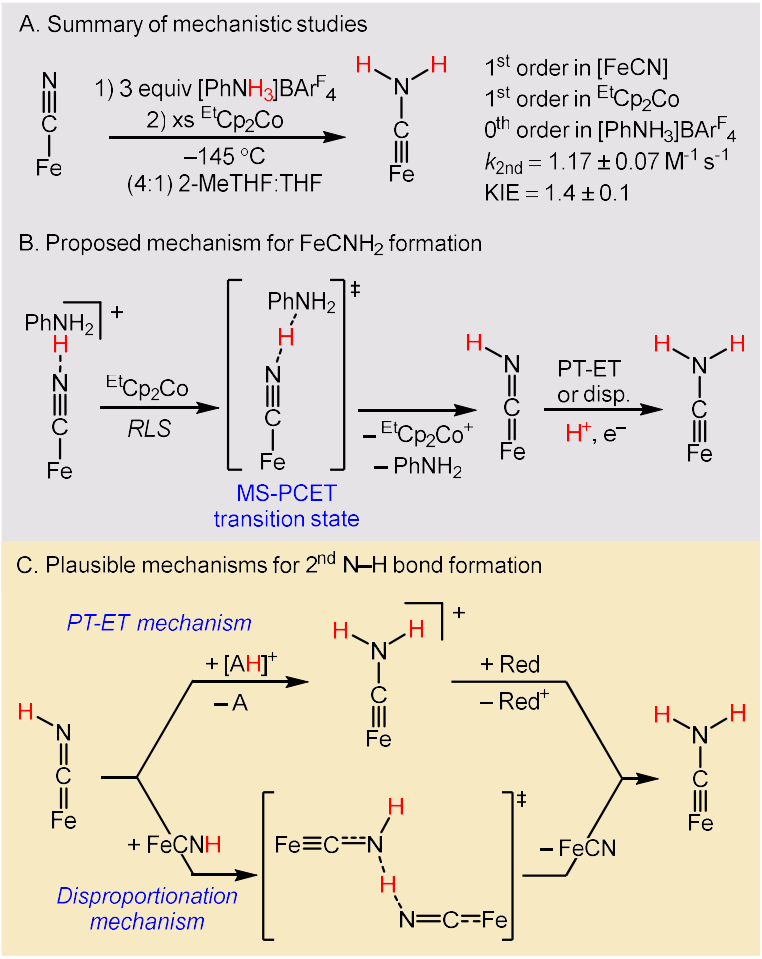

Figure 3.9. Summary of kinetic studies and proposed mechanism of 1st and 2nd N–H bond formations.

3.3 Discussion

Reversibility can be observed in the chemical and electrochemical reduction of [FeCN] to [$FeCNH_2$] (Figure 3.10). This contrast the reduction of transition metal dinitrogen complexes (M–N≡N) to the corresponding hydrazidos (M=N–NH_2), where the overpotential is limited by formation of the diazenido complex (M=N=NH). Equilibrating over multiple early intermediates would allow for lower overpotential for N_2R (and perhaps other small molecule reductions), motivating an analysis of the factors allowing for reversibility interconversion between [FeCN] and [$FeCNH_2$].

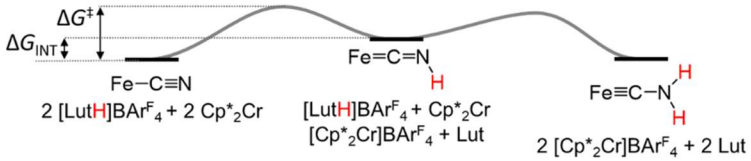

Figure 3.10. Energy diagram for reduction of [FeCN] to [$FeCNH_2$].

Two attributes of the [$FeCNH_x$] platform appear critical: small kinetic barriers for the N−H bond formation (Figure 3.10, $\Delta G^{\ddagger}$) and energy leveling (ΔG_{INT}) of the intermediate [FeCNH] and the starting material ([FeCN]) and product ([$FeCNH_2$]). The small kinetic barriers, which we attribute, at least for the 1st (and limiting) N−H bond formation, to the MS-PCET mechanism facilitated by the initial H-bond formation.[42] As noted for many MS-PCET reactions, the H-bond removes the entropic barrier of associated with the termolecular rate-limiting step.[39,40] The importance of this H-bond is readily apparent in our electrochemical studies, where formation of the H-bond pre-complex appears to be a requirement for achieving reversible transformations under electrochemical conditions.

While the design of reagents for efficient transfer of H^+/e^- to substrates is by no means trivial, strategies, particularly the tethering of H^+ and e^- donors,[42,43,57,58,59,60,61] have been detailed and demonstrated in many applications including N_2R.[62,63] By contrast, strategies for energy leveling (lowering ΔG_{INT}) between early intermediates of deep proton-coupled reductions are less well-defined, meriting further discussion. Early N−H bond formation during N_2R catalyzed by P_3^BFe (P_3^B = trisphosphinoborane ligand) specifically the conversion of the neutral dinitrogen complex ($P_3^BFe-N{\equiv}N$) to the neutral hydrazido ($P_3^BFe{=}N-NH_2$) provides a useful case study. The products and intermediates of this reaction should have the same spin states as the conversion of [FeCN] to [$FeCNH_2$]. However, the 1 H^+/ 1 e^- intermediate, the iron diazenido (P_3^BFeNNH), has a notably weaker N−H bond ($BDFE_{N-H}$ = 27 kcal mol^{-1}) than the $2H^+/2e^-$ product $P_3^BFeNNH_2$ ($BDFE_{N-H}$ = 38 kcal mol^{-1}), resulting in a large ΔG_{INT}.[64] Equilibration would require stabilizing the iron diazenido with respect to the terminal dinitrogen adduct and neutral hydrazido.

Several reports demonstrate that transition metal diazenidos can be stabilized by the addition of Lewis acids.[65,66,67,68] However, these interactions are too strong and have yielded persistent Lewis acid-stabilized diazenido species, not lower overpotentials for

N_2R (Figure 3.11A and B). To achieve lower overpotential N_2R we emphasize that the effect of a Lewis acid on the whole sequence P_3^BFeNN, P_3^BFeNNH and $P_3^BFeNNH_2$ must be considered.

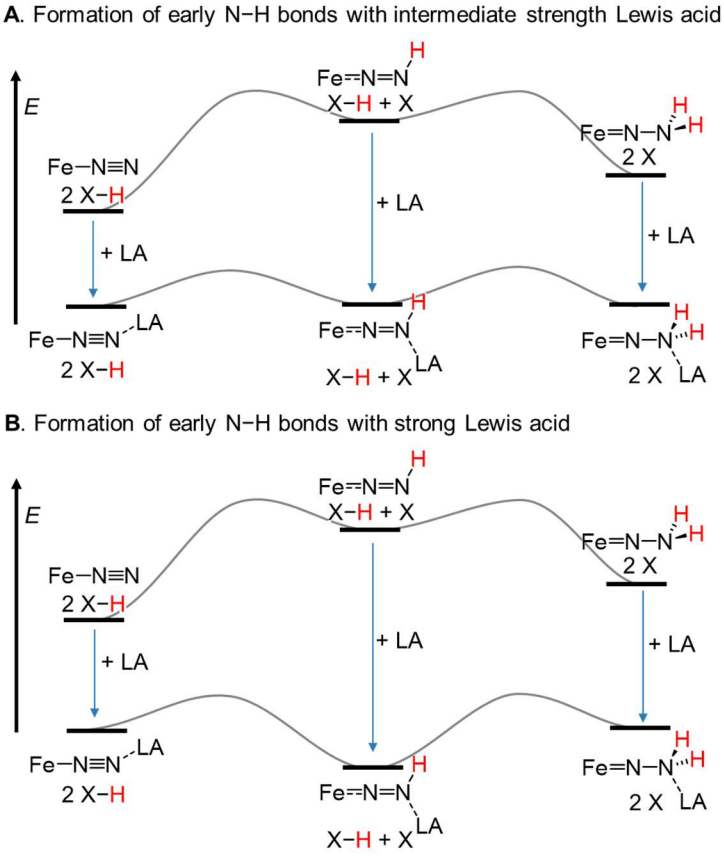

C. ECW model applied to early N−H bond in N_2R

$$-\Delta H = E_A E_B + C_A C_B + W \quad \text{(eqn 3.4)}$$

Lewis Base (L_B)	E_B	C_B	$BDFE_{N-H}$ (kcal mol^{-1})	$BDFE_{N-H}$ (L_B-Zn($NTMS_2$)$_2$) (kcal mol^{-1})	$BDFE_{N-H}$ (L_B-BMe_3) (kcal mol^{-1})
P_3^BFeNN	0.8	0	-		
P_3^BFeNNH	2.8	0.4	27	31	34
$P_3^BFeNNH_2$	2.1	0	38	35	35

Figure 3.11. Proposed energy diagrams for early steps of N_2R with intermediate (A) and strong (B) Lewis acids. For simplicity the transfer of H^+/e^- from an X−H donor is depicted.

To guide this analysis we employed the empirical ECW model of Lewis acid-base pair interactions (eqn 3.4), which estimates Lewis adduct enthalpies from $E_{A/B}$ (electrostatic) and $C_{A/B}$ (covalent) parameters, providing a useful way to classify Lewis bases both in strength and hardness/softness.[69,70] This also allows us to estimate the bond strengths of intermediates across a range of Lewis acids (see Table B.8). The computationally estimated E_B and C_B parameters for $P_3^BFe(N_2)$, $P_3^BFe(NNH)$ and $P_3^BFe(NNH_2)$, show C_B values close to 0, but larger E_B values of 0.8, 2.7 and 2.1, respectively. These E_B suggest that the iron diazenido is the strongest Lewis base, allowing for it to be stabilized relative to $P_3^BFe(NN)$ and $P_3^BFe(NNH_2)$. It also provides a guide for what Lewis acids are of an appropriate strength, with $Zn(NTMS_2)_2$ and BMe_3 being two possible candidates (Figure 3.11C).

Interestingly, comparing these computationally derived ECW parameters to other Lewis bases we find that both the diazenido and hydrazido resemble carbonyls (see Figure B.71). Lanthanide reductants, like SmI_2, have long been known to provide excellent selectivity for carbonyl-cross couplings via inner-sphere reduction.[71,72] It is therefore perhaps not surprising that lanthanide reductants have found significant utility in molecular N_2R in recent years as well.[63,73,74] Further tailoring these reagents might allow targeted energy-leveling and ultimately allow more efficient N_2R. Experiments to validate these hypotheses are underway.

3.4 Cited References

1. Bolton, J. R. *Science* **1978**. 202 (4369), 705–711.
2. Savéant, J.-M. *ACS Catal*. **2018**., 8, 7608–7611.
3. Fourmond, V.; Plumeré, N.; Léger, C. *Nat. Rev. Chem.* **2021**. 5, 348–360.
4. Hu, X.; Brunschwig, B. S.; Peters, J. C. *J. Am. Chem. Soc.* **2007**. 129, 8988–8998.
5. Smith, S. E.; Yang, J. Y.; DuBois, D. L.; Bullock, R. M. *Angew. Chem. Int. Ed.* **2012**. 51, 3152–3155.

6. Cunningham, D. W.; Barlow, J. M.; Velazquez, R. S.; Yang, J. Y. *Angew. Chem. Int. Ed.* **2020**. 59, 4443–4447.
7. Guria, S.; Dolui, D.; Das, C.; Ghorai, S.; Vishal, V.; Maiti, D.; Lahiri, G. K.; Dutta, A. *Nat. Commun.* **2023**. 14, 6859.
8. Suzuki, W.; Kotani, H.; Ishizuka, T.; Kojima, T. *J. Am. Chem. Soc.* **2019**. 141, 5987–5994.
9. Rodriguez, G. M.; Trotta, C.; Tensi, L.; Macchioni, A. *J. Am. Chem. Soc.* **2024**. 146, 34298–34303
10. Eftekhari, A. *Int. J. Hydrog. Energy* **2017**. 42, 11053–11077.
11. Kortlever, R.; Peters, I.; Koper, S.; Koper, M. T. M. *ACS Catal*. **2015**. 5, 3916–3923.
12. Hexter, S. V.; Grey, F.; Happe, T.; Climent, V.; Armstrong, F. A. *Proc. Natl. Acad. Sci.* **2012**. 109, 11516–11521.
13. Can, M.; Armstrong, F. A.; Ragsdale, S. W. *Chem. Rev.* **2014**. 114, 4149–4174.
14. Bassegoda, A.; Madden, C.; Wakerley, D. W.; Reisner, E.; Hirst, J. *J. Am. Chem. Soc.* **2014**. 136, 15473–15476.
15. Reda, T.; Plugge, C. M.; Abram, N. J.; Hirst, J. *Proc. Natl. Acad. Sci.* **2008**. 105, 10654–10658.
16. Yandulov, D. V.; Schrock, R. R. *Science* **2003**. 301, 76–78.
17. Chalkley, M. J.; Drover, M. W.; Peters, J. C. *Chem. Rev.* **2020**. 120, 5582–5636.
18. Ritleng, V.; Yandulov, D. V.; Weare, W. W.; Schrock, R. R.; Hock, A. S.; Davis, W. M. *J. Am. Chem. Soc.* **2004**. 126, 6150–6163.
19. Wu, Y.; Jiang, Z.; Lu, X.; Liang, Y.; Wang, H. *Nature* **2019**. 575, 639–642.
20. Boutin, E.; Wang, M.; Lin, J. C.; Mesnage, M.; Mendoza, D.; Lassalle-Kaiser, B.; Hahn, C.; Jaramillo, T. F.; Robert, M. *Angew. Chem. Int. Ed.* **2019**. 58, 16172–16176.
21. Tanifuji, K.; Lee, C. C.; Ohki, Y.; Tatsumi, K.; Hu, Y.; Ribbe, M. W. *Angew. Chem. Int. Ed.* **2015**. 54, 14022–14025.

22. Sickerman, N. S.; Tanifuji, K.; Lee, C. C.; Ohki, Y.; Tatsumi, K.; Ribbe, M. W.; Hu, Y. *J. Am. Chem. Soc.* **2017**. 139, 603–606.
23. Johansen, C. M.; Peters, J. C. *J. Am. Chem. Soc.* **2024**. 146, 5343–5354.
24. Habibzadeh, F.; Miller, S. L.; Hamann, T. W.; Smith, M. R. *Proc. Natl. Acad. Sci.* **2019**. 116, 2849–2853.
25. Zott, M. D.; Garrido-Barros, P.; Peters, J. C. *ACS Catal.* **2019**. 9, 10101–10108.
26. Trenerry, M. J.; Wallen, C. M.; Brown, T. R.; Park, S. V.; Berry, J. F. *Nat. Chem.* **2021**. 13, 1221–1227.
27. Brownell, K. R.; McCrory, C. C. L.; Chidsey, C. E. D.; Perry, R. H.; Zare, R. N.; Waymouth, R. M. *J. Am. Chem. Soc.* **2013**. 135, 14299–14305.
28. Liu, Y.; Zhao, S.-F.; Guo, S.-X.; Bond, A. M.; Zhang, J.; Zhu, G.; Hill, C. L.; Geletii, Y. V. *J. Am. Chem. Soc.* **2016**. 138, 2617–2628.
29. Chen, C.-P.; Alharbi, W.; Cundari, T. R.; Hamann, T. W.; Smith, M. R. I. *J. Am. Chem. Soc.* **2023**. 145, 26339–26349.
30. Wang, Z.; Johnson, S. I.; Wu, G.; Ménard, G. *Inorg. Chem.* **2021**. 60, 8242–8251.
31. Huynh, M. H. V.; Meyer, T. J. *Chem. Rev.* **2007**. 107, 5004–5064.
32. Pipes, D. W.; Meyer, T. J. *J. Am. Chem. Soc.* **1984**. 106, 7653–7654.
33. Huynh, M. H. V.; Baker, R. T.; Morris, D. E.; White, P. S.; Meyer, T. J. *Angew. Chem. Int. Ed.* **2002**. 41, 3870–3873.
34. L. Hughes, D.; K. Ibrahim, S.; Moh'd Ali, H.; J. Pickett, C. *J. Chem. Soc. Chem. Commun.* **1994**. 4, 425–427.
35. Rittle, J.; Peters, J. C. *Angew. Chem. Int. Ed.* **2016**, 55, 12262–12265.
36. Rittle, J.; Peters, J. C. *J. Am. Chem. Soc.* **2017**. 139, 3161–3170.
37. Chalkley, M. J.; Peters, J. C. *Eur. J. Inorg. Chem.* **2020**. 2020, 1353–1357.
38. Pombeiro, A. J. L. *Inorg. Chem. Commun.* **2001**. 4, 585–597.
39. Morris, W. D.; Mayer, J. M. *J. Am. Chem. Soc.* **2017**. 139, 10312–10319.
40. Gentry, E. C.; Knowles, R. R. *Acc. Chem. Res.* **2016**, 49, 1546–1556.

41. Waidmann, C. R.; Miller, A. J. M.; Ng, C.-W. A.; Scheuermann, M. L.; Porter, T. R.; Tronic, T. A.; Mayer, J. M. *Energy Environ. Sci.* **2012**, 5, 7771–7780.
42. Tyburski, R.; Liu, T.; Glover, S. D.; Hammarström, L. *J. Am. Chem. Soc.* **2021**, 143, 560–576.
43. Agarwal, R. G.; Coste, S. C.; Groff, B. D.; Heuer, A. M.; Noh, H.; Parada, G. A.; Wise, C. F.; Nichols, E. M.; Warren, J. J.; Mayer, J. M. *Chem. Rev.* **2022**. 122, 1–49.
44. Bordwell, F. G.; Cheng, J. Pei.; Harrelson, J. A. *J. Am. Chem. Soc.* **1988**. 110, 1229–1231.
45. Previously measured pK_a of [FeCN] measured in THF with TfO^- counteranion at 25°C did not result in observable H-bonding interactions with $[Et_3NH]OTf$ or [LutH]OTf , see ref 36.
46. Garrido, G.; Rosés, M.; Ràfols, C.; Bosch, E. *J. Solut. Chem.* **2008**. 37, 689–700.
47. Connelly, N. G.; Geiger, W. E. *Chem. Rev.* **1996**. 96, 877–910.
48. Interestingly, the linewidth for the Mössbauer spectra generated with $[PhNH_3]BAr^F{}_4$ are much broader than those generated with $[LutH]BAr^F{}_4$. We attribute this to H-bonding between the conjugate base and $[FeCNH_2]$, the bulkier lutidine base allows fewer modes of H-bonding and accordingly more narrow speciation and sharper linewidths.
49. It is worth commenting on the discrepancy in the 1:1 ratio of starting material:product observed compared to the 3:97 ratio expected at 195 K for an energy difference of −1 kcal mol^{-1}, which is attributable to a variety of effects. As these driving force equations do not directly relate to $[FeCNH_2]$ as the BDFE of the neutral carbyne is measured for [FeCN(Me)H]. In addition, there are hydrogen bonding effects in both starting material and product, which are not accounted for in these simple driving force calculations.

50. Since ΔG = +2 kcal mol^{-1}, a larger excess acid and reductant was required to form appreciable [FeCNH$_2$], allowing product detection by ^{57}Fe Mössbauer.
51. Efforts to synthesize this complex in Et$_2$O failed, likely due to insolubility of [FeCN]K$_2$, with invariably substantial oxidation to [FeCN]K or [FeCNH$_2$]$^+$ observed, prompting the switch to THF solvent for the oxidative reaction.
52. Chalkley, M. J.; Del Castillo, T. J.; Matson, B. D.; Roddy, J. P.; Peters, J. C. *ACS Cent. Sci.* **2017**. 3, 217–223.
53. Steiner, T. *Angew. Chem. Int. Ed.* **2002**. 41, 48–76.
54. When using strong acid (e.g., [Ph$_2$NH$_2$]BAr$^F_4$ or [$^{2\text{-Cl}}$PhNH$_3$]BAr$^F_4$) or strong reductant (Cp$^*_2$Co) [FeCN] reduction occurs via either PT or ET first mechanisms evidenced by full or partial formation of [FeCNH]$^+$ or [FeCN]$^-$ with these reagents.
55. Chiang, L.; Keown, W.; Citek, C.; Wasinger, E. C.; Stack, T. D. P. *Angew. Chem. Int. Ed.* **2016**. 55, 10453–10457.
56. As [FeCNH] is unstable we have not been able to determine its reduction potential electrochemically, but use the methylated analogue gives a reasonable estimate of the [FeCNH]$^{0/-}$ reduction potential.
57. Chalkley, M. J.; Garrido-Barros, P.; Peters, J. C. *Science* **2020**. 369, 850–854.
58. Anson, C. W.; Stahl, S. S. *J. Am. Chem. Soc.* **2017**. 139, 18472–18475.
59. Boyd, E. A.; Peters, J. C. *J. Am. Chem. Soc.* **2022**. 144, 21337–21346.
60. Dey, S.; Masero, F.; Brack, E.; Fontecave, M.; Mougel, V. *Nature* **2022**. 607, 499–506.
61. Adillon, E. H.; Peters, J. C. *J. Am. Chem. Soc.* **2024**. 146, 30204–30211.
62. Garrido-Barros, P.; Derosa, J.; Chalkley, M. J.; Peters, J. C. *Nature* **2022**. 609, 71–76.
63. Boyd, E. A.; Peters, J. C. *J. Am. Chem. Soc.* **2023**. 145 (27), 14784–14792.
64. Matson, B. D.; Peters, J. C. *ACS Catal.* **2018**, 8, 1448–1455.

65. Geri, J. B.; Shanahan, J. P.; Szymczak, N. K. *J. Am. Chem. Soc.* **2017**. 139, 5952–5956.

66. Ouellette, E. T.; Magdalenski, J. S.; Bergman, R. G.; Arnold, J. *Inorg. Chem.* **2022**. 61, 16064–16071.

67. Rempel, A.; Mellerup, S. K.; Fantuzzi, F.; Herzog, A.; Deißenberger, A.; Bertermann, R.; Engels, B.; Braunschweig, H. *Chem. – Eur. J.* **2020**. 26, 16019–16027.

68. Yin, Z.-B.; Wang, G.-X.; Yan, X.; Wei, J.; Xi, Z. *Nat. Commun.* **2025**, 16, 674.

69. Drago, R. S.; Wayland, B. B. *J. Am. Chem. Soc.* **1965**. 87, 3571–3577.

70. Vogel, G. C.; Drago, R. S. *J. Chem. Educ.* **1996**. 73, 701.

71. Girard, P.; Namy, J. L.; Kagan, H. B. *J. Am. Chem. Soc.* **1980**. 102, 2693–2698.

72. Szostak, M.; Fazakerley, N. J.; Parmar, D.; Procter, D. J. *Chem. Rev.* **2014**. 114, 5959–6039.

73. Ashida, Y.; Arashiba, K.; Nakajima, K.; Nishibayashi, Y. *Nature* **2019**. 568, 536–540.

74. Boyd, E. A.; Jung, H.; Peters, J. C. *J. Am. Chem. Soc.* **2025**. 147, 4695–4700.